

An atmospheric energy-moisture balance model: climatology, interpentadal climate change, and coupling to an ocean general circulation model

Augustus F. Fanning and Andrew J. Weaver

School of Earth and Ocean Sciences, University of Victoria, Victoria, British Columbia, Canada

Abstract.

An atmospheric model incorporating energy and moisture balance equations is developed for use in process studies of the climate system. Given the sea surface temperature and specified surface wind field, the atmospheric model calculates the surface fields of air temperature, specific humidity, as well as heat and freshwater fluxes. The inclusion of the moisture balance in the atmospheric model allows the effects of latent heat transport to be included explicitly in the model. Under fixed climatological sea surface temperature (SST) and surface wind conditions, surface air temperatures, specific humidities, and surface fluxes are comparable to direct estimates. Precipitation compares less favorably with observations. As an extension to the climatological forcing case, we conduct a simple perturbation experiment in which the 1955–1959 pentad is compared to the 1970–1974 pentad by driving the model under the respective SST fields. The model exhibits a global air temperature decrease in the latter pentad of 0.27°C (comparable to direct estimates) with cooling in the northern hemisphere and warming in the southern hemisphere. Such large-scale cooling in our atmospheric model is driven by equivalent local changes in the prescribed SST fields, subsequently smoothed by atmospheric diffusion of heat. The interpentadal modeled differences are shown to be quite robust through model experiments using parameters representative of several different unrealistic climatologies. The resulting interpentadal difference fields change remarkably little even when the background state has changed dramatically. This emphasizes the almost linear response of the atmospheric model to the imposed SST changes. The atmospheric model is also coupled to an ocean general circulation model without the need for flux adjustments. This coupled climate model faithfully represents deep water formation in the North Atlantic and Southern Ocean, with upwelling throughout the Pacific and Indian Oceans. Water mass characteristics in the vertical compare very favorably with direct observations.

1. Introduction

In ocean circulation modeling, information on large-scale air-sea interactions is necessary to provide boundary conditions for model integration. Options for specifying the surface forcing include fluxes derived from observational data and those from atmospheric general circulation models. Unfortunately, the paucity of observational data over the oceans often prohibits the use of prescribed surface fluxes, while the complexity as well as computational cost often prohibits the use of fully coupled ocean-atmosphere schemes. Consequently, the most prevalent scheme utilized by ocean modelers is a Newtonian restoring boundary condition in which the

heat and salt fluxes (Q_H, Q_S) are implied by restoring to observed (or apparent) sea surface temperature (SST) and sea surface salinity (SSS):

$$Q_H = \gamma_H(T_1 - T^*); \quad Q_S = \gamma_S(S_1 - S^*) \quad (1)$$

where (T_1, S_1) , (T^*, S^*) are the ocean model's and observed (or apparent) surface temperature and salinity, respectively, and (γ_H, γ_S) are the exchange coefficients for heat and salt. While the use of (1) may be adequate for achieving an oceanic equilibrium state, its basic assumptions preclude its use in studying the ocean's role in climate change/climate variability. In process studies of the ocean's role in climate change, mixed boundary conditions are often employed in which the salt flux is fixed, while the restoring condition on temperature is maintained. It is widely recognized that such an approach also has serious deficiencies in its representation of the atmospheric state. While the use of a restor-

Copyright 1996 by the American Geophysical Union.

Paper number 96JD01017.
0148-0227/96/96JD-01017\$09.00

ing condition on SST allows for changes in the surface heat flux due to changes in the oceanic state, the implied changes in fluxes are generally too strong [Zhang *et al.*, 1993; Power and Kleeman, 1994; Tziperman *et al.*, 1994; Mikolajewicz and Maier-Reimer, 1994; Rahmstorf and Willebrand, 1995]. In addition, the use of a fixed salt flux does not allow for changes in the latent heat flux from the ocean (evaporation) or changes in latent heat transport (and hence precipitation) associated with changes in the oceanic state [*e.g.*, Huang, 1993; Hughes and Weaver, 1996].

The primary focus of this paper is to develop a simple atmospheric model for use in process-oriented coupled ocean-atmosphere studies of the ocean's role in climate change and variability. Since timescales of variability associated with atmospheric processes are generally short compared to the oceanic timescales of interest (decadal to century), we appeal to a simple diffusive energy-moisture balance model for our atmospheric processes. It is worth pointing out, however, that the assumption of diffusive transport is only valid for timescales greater than annual and for length scales greater than 10^6 m [Lorenz, 1979].

The energy-moisture balance model's strength lies in its simplicity and computational efficiency. The model relates all components of the atmospheric system to only three variables: surface air temperature, sea surface temperature, and specific humidity. When coupled to an ocean general circulation model (OGCM), a good simulation of the present climate is obtained (under present-day forcing and without flux corrections).

The outline of the rest of this paper is as follows: in section 2 we introduce our atmospheric model, its numerical implementation, as well as our rationale for the choice of model parameters. In section 3 we present the modeled climatology under fixed SST and wind speed, including surface fluxes, temperature, and specific humidity; we also explore the model's sensitivity to its internal parameters. Section 4 presents interpentadal climate differences obtained by prescribing the pentadal SST for 1955-1959, and 1970-1974 [Levitus, 1989], along with a test of the sensitivity of changes to the background climatology. In section 5 we present results from an integration in which the energy-moisture balance model is coupled to an ocean general circulation model. Finally, a summary and discussion are presented in section 6.

2. Atmospheric Model

2.1 Model Equations

The energy-moisture balance climate model we employ is thermodynamically related to the earlier models of Budyko [1969], Sellers [1969], and North [1975a]. We have extended these models to allow coupling to the oceanic state by allowing latent, sensible, and radiative heat transfers between the ocean and the atmosphere.

The atmospheric energy balance, over the ocean, is expressed by

$$\rho_{\text{air}} H_{\text{air}} C_{\rho a} \frac{\partial T_{\text{air}}}{\partial t} = Q_T + Q_{\text{SSW}} - Q_{\text{LW}} + Q_{\text{RR}} + Q_{\text{SH}} + Q_{\text{LH}} \quad (2a)$$

while over land, we have

$$\rho_{\text{air}} H_{\text{air}} C_{\rho a} \frac{\partial T_{\text{air}}}{\partial t} = Q_T + Q_{\text{SSW}} - Q_{\text{LW}} + Q_{\text{LH}} \quad (2b)$$

where ρ_{air} is a constant surface air density, $C_{\rho a}$ the specific heat of air at constant pressure, H_{air} a constant scale height representative of the atmosphere, and T_{air} is the surface air temperature. The terms arising on the right-hand side of (2) are the eddy-diffusive horizontal heat transport, Q_T ; the absorbed atmospheric shortwave radiation, Q_{SSW} ; the planetary longwave flux, Q_{LW} ; the surface longwave flux, Q_{RR} ; the surface sensible heat flux, Q_{SH} ; and the atmospheric latent heat flux, Q_{LH} .

The eddy-diffusive horizontal heat transport parameterization is given by

$$Q_T = \rho_{\text{air}} H_{\text{air}} C_{\rho a} \nabla \cdot (\nu \nabla T_{\text{air}}) \quad (3)$$

in which ν is a latitudinally dependent heat transport coefficient meant to represent processes associated with baroclinic eddies and the Hadley cell [Lindzen and Farrell, 1977, 1980].

In general, the atmosphere is an inefficient absorber of incoming shortwave radiation, although water vapor, dust, ozone, and clouds may absorb upwards of 30% of the total [Ramanathan, 1987]. To mimic this effect, we apply a source term in the atmosphere:

$$Q_{\text{SSW}} = \frac{S_{\odot}}{4} S(1 - \alpha)(1 - C_0) \quad (4)$$

where S_{\odot} is the solar constant, S is the annual distribution of shortwave radiation intersecting the top of the atmosphere, α is the latitudinally dependent albedo, and C_0 is a reduction parameter representing the scattering/absorption processes described above. Over land, all shortwave radiation intercepted is assumed returned (via black body radiation) to the atmosphere so that C_0 assumes a value of zero there.

The net longwave relaxation to space is modeled by considering the planet as a gray body with emissivity ϵ_P . The infrared emission is then given by

$$Q_{\text{LW}} = \epsilon_P \sigma T_{\text{air}}^4 \quad (5a)$$

where σ is the Stefan-Boltzmann constant. This formulation differs from that of the Budyko [1969], Sellers [1969], and North [1975a] models where a linear approximation

$$Q_{\text{LW}} = A + B T_{\text{air}} \quad (5b)$$

was employed. In these earlier models, satellite observations constrained A and B to an order of magnitude, but

they required tuning to the modeled temperature distribution. Here we objectively determine ε_P and maintain it to its zonally averaged form, as discussed in section 2.2.

The longwave radiation emitted by the ocean is strongly absorbed by greenhouse gases present in the atmosphere. The atmosphere then reemits this absorbed energy both upward and downward resulting in a longwave flux at the ocean-atmosphere interface, which we model as a gray body emission. The radiative flux is written as

$$Q_{RR} = \varepsilon_O \sigma T_{sea}^4 - \varepsilon_A \sigma T_{air}^4 \quad (6)$$

where T_{sea} is the sea surface temperature and $\varepsilon_O, \varepsilon_A$ are the oceanic and atmospheric emissivities.

A traditional bulk parameterization is utilized for the sensible heat flux from the ocean:

$$Q_{SH} = \rho_{air} C_H C_{pa} U (T_{sea} - T_{air}) \quad (7)$$

where C_H is the Stanton number, and U is the surface scalar wind speed. The latent heat flux into the atmosphere takes the form

$$Q_{LH} = \frac{\rho_{sea}}{s/yr} L_\nu P \quad (8)$$

where L_ν is the latent heat of evaporation, s/yr is the number of seconds in a year, and P is the precipitation (in meters per year).

We obtain a parameterization of the hydrological cycle by considering an approximation to the balance equation for water vapor in the atmosphere in which we replace the horizontal advection terms by an eddy diffusive term. Vertically integrating over the depth of the atmosphere, we obtain

$$\rho_{air} H_q \frac{\partial q_{air}}{\partial t} = M_T + \frac{\rho_{sea}(E - P)}{s/yr} \quad (9)$$

where M_T is the eddy-diffusive horizontal moisture transport parameterization

$$M_T = \rho_{air} H_q \nabla \cdot (\kappa \nabla q_{air}) \quad (10)$$

where H_q is a constant scale height depth for the specific humidity, q_{air} , κ is an eddy diffusive horizontal redistribution term; P is the precipitation, and E is the evaporation (both in meters per year). The evaporation is calculated from its traditional bulk formula

$$E = \frac{\rho_{air} C_E U s/yr}{\rho_{sea}} (q_{sat}(T_{sea}) - q_{air}) \quad (11)$$

where C_E is the Dalton number, $q_{sat}(T_{sea})$ is the saturation specific humidity at T_{sea} (calculated from the Clausius-Clapeyron equation and utilizing the empirical formula of Bolton [1980]). Traditionally, a constant humidity is used in the bulk parameterization for the evaporation [e.g., Haney, 1971]; however, since we also consider the conservation of water vapor, this is not necessary in the present formulation.

To obtain closure of (9), we parameterize the precipitation as

$$P = \frac{\rho_{air} H_q s/yr}{\rho_{sea} \tau} H(r) (q_{air} - .85 q_{sat}(T_{air})) \quad (12)$$

where τ is the model time step, $q_{sat}(T_{air})$ is the saturation specific humidity at T_{air} , r is the relative humidity, and

$$H(r) = \begin{cases} 1, & \text{if } r \geq 85\%; \\ 0, & \text{otherwise} \end{cases} \quad (13)$$

The evaporation is treated explicitly in (9). At the end of a time step, if the relative humidity exceeds 85%, precipitation occurs and the specific humidity is lowered to its 85% saturation value, which is then utilized in computing the evaporation for the next time step.

The net heat flux into the ocean (presented in section 3.1) is defined as

$$Q_H = Q_{SW} - Q_{SH} - Q_{RR} - Q_{LH} \quad (14)$$

where Q_{SW} is the incoming shortwave radiation, expressed as

$$Q_{SW} = \frac{S_\odot}{4} S(1 - \alpha) C_0 \quad (15)$$

The definitions of Q_{SH} and Q_{RR} are the same as those in (6) and (7), while the latent heat flux out of the ocean takes the form

$$Q_{LH} = \frac{\rho_{sea}}{s/yr} L_\nu E \quad (16)$$

and the freshwater flux over the ocean takes the form

$$Q_S = (E - P) \quad (17)$$

In the present study, the landmass is assumed to be inactive. In this context there is no heat or moisture storage on the landmass, and latent and sensible heat fluxes from the land are zero, an assumption valid for the climatological and interannual time scales we consider. Precipitation and hence latent heat release into the atmosphere can occur over the landmass, with all precipitation returning to the ocean via major river drainage basins as detailed in Figure 6 of *Weaver and Hughes* [1996].

The numerical solutions of (2) and (9) are calculated on the Arakawa Bgrid. The time derivatives are treated by leapfrog-in-time differencing (the computational mode is suppressed by an occasional forward Euler time step), while the eddy diffusion terms are integrated using an Euler backward time step, and the forcing terms utilize centered-in-time finite differences. The results presented in sections 3-5 are performed on a global domain, with a cyclic east-west boundary condition, while a no-normal flux condition is applied at the northern and southern extents of the model domain. The numerical solution is achieved at minimal computational cost by utilizing a generalized minimum residual iteration [Seager, 1988]. Treating the eddy diffusion terms implicitly allows for a time step of roughly a half day (for the leap-frog time step), and a quarter day (for

Table 1. Summary of Model Parameters and Sources

Parameter	Description	Value	Source
a	radius of the Earth	6371 km	NA
$(1 - \alpha)$	coalbedo	see Figure 2d	<i>Graves et al.</i> [1993]
ρ_{air}	surface air density	1.25 kg/m ³	NA
ρ_{sea}	sea surface density	1024 kg/m ³	NA
C_E	Dalton number	see Figure 3	<i>Isemer et al.</i> [1989]
C_H	Stanton number	$0.94C_E$	<i>Isemer et al.</i> [1989]
C_0	solar scattering coefficient	see Figure 2c	<i>da Silva et al.</i> [1994b]
$C_{\rho a}$	heat capacity of dry air	10 ³ J/(kgK)	NA
ε_A	atmospheric emissivity	see Figure 2a	<i>da Silva et al.</i> [1994a, b]
ε_P	planetary emissivity	see Figure 2b	<i>da Silva et al.</i> [1994a]
ε_O	oceanic emissivity	0.96	<i>Isemer et al.</i> [1989]
H_a	atmospheric scale depth	8400 m	<i>Gill</i> [1982]
H_q	specific humidity scale depth	1800 m	<i>Peixoto and Oort</i> [1992]
κ	eddy diffusivity for moisture	see Figure 1	present study
L_ν	latent heat of evaporation	2.5×10^6 J/kg	NA
ν	eddy diffusivity for heat	see Figure 1	present study
S	solar insolation distribution	...	<i>North</i> [1975b]
S_\odot	solar constant	1360 W/m ²	NA
τ	model time step	0.5 (0.25) days	present study
σ	Stefan-Boltzmann constant	5.67×10^{-8} W/(m ² K ⁴)	NA

the forward time step). By comparison, an earlier version of the model with explicit diffusion required a time step of roughly ten minutes.

2.2. Model Parameters

As has already been mentioned, the results to be presented in section 3 comprise a global simulation of the atmospheric climatology inferred by running our model to equilibrium with the oceanic SST and wind speed set to *Levitus* [1982], and *da Silva et al.* [1994b], respectively. A number of parameters must be specified in an effort to simulate the present climatology (the reader is referred to Table 1 for a complete listing of values and/or sources). In the present study we have drawn upon previous works for many of our parameters with an eye toward both simplicity and physical justification. To this end we have retained only the latitudinal variation of parameters, our only justification for this being model simplicity. Although a number of physical and dynamical processes which are not included in this model (e.g., cloud or land surface processes) could indeed be synthesized by detailed spatial parameterizations, we take the view that such "fine tuning" of the model ultimately prohibits its use over a wide range of applications.

Figure 1 depicts the heat (ν) and moisture (κ) latitudinal diffusivities used in the atmospheric transport terms. As has been pointed out, the latitudinal profile of ν is justified by *Lindzen and Farrell* [1977, 1980] and is that utilized by *North et al.* [1983], although here we utilize a lower value (roughly 60%) since the spec-

ified *Levitus* [1982] SST implicitly implies an oceanic heat transport once air-sea fluxes are determined. To define the latitudinal profile for moisture diffusion (κ), we utilized observational estimates of $E - P$ and integrated the steady state, zonally averaged form of (9). While such an integral constrains the general shape and magnitude of κ , slight errors (accumulated during integration) can radically modify the profile. Hence we symmetrized the profile about the equator and tuned the final profile to match observational evidence that E dominates over P at midlatitudes, while precipitation dominates at high latitudes. By comparison with observed northward and eastward water vapor transport [see *Peixoto and Oort*, 1992, Figures 12.9, 12.12] this is a good approximation for large-scale atmospheric and stationary-eddy motions, with the exception of the Intertropical Convergence Zone (ITCZ). Comparing with

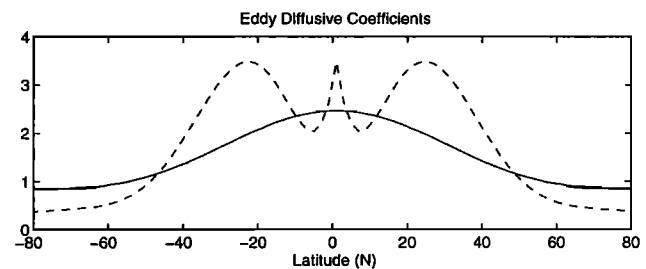


Figure 1. Latitudinal profile of the heat diffusion coefficient, ν (solid line), and the moisture diffusion coefficient, κ (dashed line). Units are 10^6 m²/s.

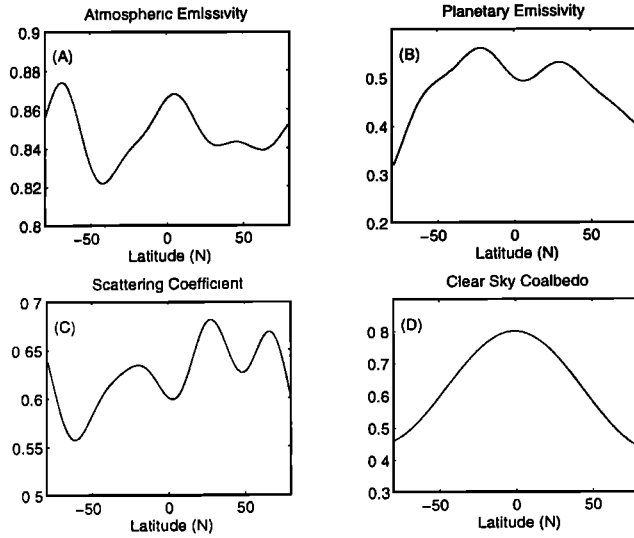


Figure 2. (a) Latitudinal profile of the atmospheric emissivity, ϵ_A . (b) As in Figure 2a but showing the planetary emissivity, ϵ_P . (c) As in Figure 2a but showing the scattering coefficient, C_0 . (d) As in Figure 2a but showing the applied coalbedo ($1 - \alpha$) of *Graves et al.* [1993].

the zonal-mean transport of water vapor [see *Peiróto and Oort*, 1992, Figure 12.18], diffusive transport is valid poleward of roughly 20° , within the ITCZ, however, the transport is up-gradient. The use of a negative diffusion coefficient within this region could mimic this phenomenon; however, the solution technique we employ (which allows the model's efficient implementation and solution) breaks down when a negative diffusion coefficient is employed. We therefore trade resolution of the ITCZ for numerical efficiency. This also explains the peak in κ at the equator; we still require the strong smoothing of the specific humidity field the ITCZ would provide.

The atmospheric emissivity (see Figure 2a) is determined by fitting (6) to the *da Silva et al.* [1994b] zonally averaged net longwave flux (an oceanic emissivity of 0.96 [Isemer et al., 1989], and the *Levitus* [1982] zonally averaged SST data are also employed). The planetary emissivity (see Figure 2b) has been inferred by fitting (5) to the *Campbell and Vonder Haar* [1980] planetary longwave flux using the zonally averaged climatological surface air temperature based on the Comprehensive Ocean-Atmosphere Data Set (COADS) analysis of *da Silva et al.* [1994a]. The objectively determined planetary emissivity (ϵ_P) is consistent with values utilized by *Stocker et al.* [1992], although it is somewhat lower toward the poles. Notice that the planetary emissivity varies a great deal with latitude and is lower than the atmospheric emissivity at all latitudes. This is related to the simplistic planetary infrared flux we employ. Top of the atmosphere longwave flux is made up of a combination of emittance from the surface of the planet and infrared absorbing materials in the atmospheric column

(e.g., water vapor, liquid, ice). In this respect, the planetary emissivity is lower than the atmospheric emissivity to account for the fact the emittance comes from higher in the atmosphere.

The scattering coefficient we employ is also derived from the COADS analysis of *da Silva et al.* [1994b]. Their incoming shortwave radiation is used (along with (4)) to infer C_0 , (see Figure 2c). The scattering acts to filter roughly 30% of the incoming shortwave radiation, consistent with the 20 – 30% estimated from the radiation balance for the Earth, [Ramanathan, 1987]. Finally, Figure 2d indicates the latitudinal profile of the annual coalbedo ($1 - \alpha$) as derived by *Graves et al.* [1993] from the Earth Radiation Budget Experiment data.

In practice, the bulk transfer coefficients C_E and C_H (the Dalton and Stanton numbers) are often taken as constants of the same magnitude ($\sim 1.3 \times 10^{-3}$). The bulk transfer coefficients are in actuality dependent on the wind speed, air temperature, SST, and relative humidity. Indeed, through fine tuning of the bulk transfer coefficients, heat flux estimates can be constrained for use in ocean modeling [e.g. *Isemer et al.*, 1989]. In an effort to consistently apply the bulk transfer coefficients, we considered the best linear fit (in a least squares sense) to wind speed, and air-sea temperature difference [see *Isemer et al.*, 1989, Table 2]. The resulting equations for the Dalton and Stanton numbers are then given by

$$6.0 \times 10^{-5} \leq C_E = 1.0 \times 10^{-3}(1.0022 - .0822(T_{\text{air}} - T_{\text{sea}}) + .0266U) \leq 2.19 \times 10^{-3} \quad (18)$$

$$C_H = 0.94C_E \quad (19)$$

In this manner the exchange coefficients are capable of adjusting (during the model integration) to changes in the modeled air-sea temperature difference. The zonally averaged climatological Dalton number obtained from our model integration is shown in Figure 3. The global mean value of 1.26×10^{-3} compares well with observationally derived estimates [e.g., *Large and Pond*, 1982; *Smith*, 1988], and the profile is also consistent with the estimates of *Hsiung* [1986] and *Oberhuber* [1988].

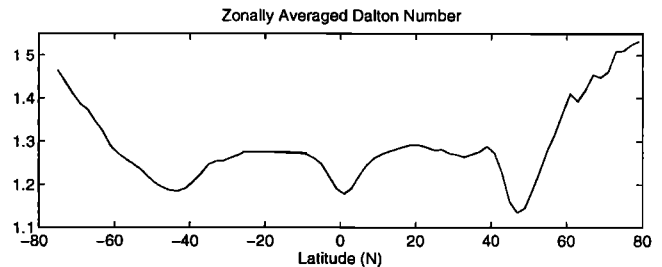


Figure 3. Zonally averaged model-derived Dalton number, C_E . The Stanton number can be obtained by $C_H = 0.94C_E$.

2.3. Uncertainty in Model Parameters

The parameters described in the previous section have been empirically determined from a particular set of observations. Their values would be slightly different if a different sample of observations (or bulk formulae) were prescribed. Here we attempt to place limits upon the uncertainty associated with our model parameters. While the large number of observations utilized in defining a climatological annual mean field would tend to minimize the uncertainty (as would the zonal averaging we employ), objective analysis procedures employed (as in the works of *Levitus* [1982] and *da Silva et al.* [1994a,b,c, and d]) as well as the “fair weather bias” in data collection introduce an unquantifiable uncertainty. To this end, the uncertainty we define below is somewhat speculative and should be viewed merely as a first-order estimate.

Blanc [1987] indicates the rms uncertainty in surface air temperature is 0.6 K, while *Peixoto and Oort* [1992] indicate that the *Campbell and Vonder Haar* [1980] planetary longwave flux has an uncertainty of 10 W/m^2 , indicating an rms uncertainty of 5% in our planetary emissivity ϵ_P (see (5a)). *Fung et al.* [1984] compared eight different bulk formulae for the net oceanic longwave flux. Their results suggest a $10\text{--}15 \text{ W/m}^2$ uncertainty associated with the use of various bulk formulae. This, together with the roughly 0.6 K uncertainty in the air/sea surface temperatures, results in an rms uncertainty in the atmospheric emissivity ϵ_A (see (6)) of roughly 4.4%.

Comparing three different parameterizations of the shortwave radiation reaching the ocean surface suggests an uncertainty of approximately 15 W/m^2 (or roughly 8.6%). If we assume the *Graves et al.* [1993] coalbedo has an associated uncertainty of 5% (consistent with the uncertainty in *Campbell and Vonder Haar*’s satellite-derived outgoing longwave radiation estimate), we obtain an rms uncertainty of 10% in the scattering coefficient C_0 utilized in (4) and (15).

Finally, *Blanc* [1987] indicates a 10% rms uncertainty in ship-derived surface wind speeds due to sensor error

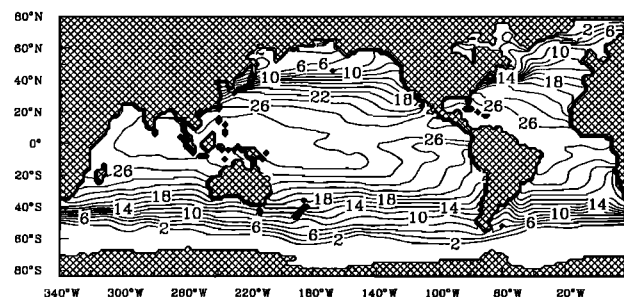


Figure 4. Climatological sea surface temperature (SST) specified as the model’s lower boundary condition, from *Levitus* [1982]. Shaded regions indicate land. The contour interval is 2°C , with dashed contours indicating negative values.

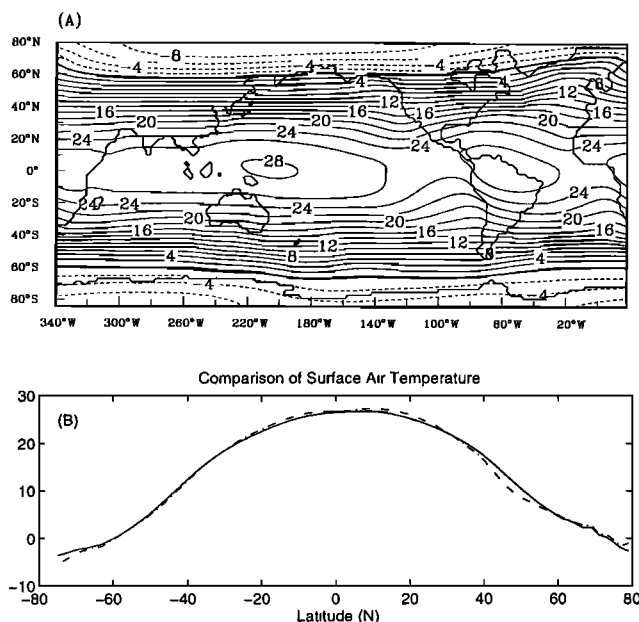


Figure 5. (a) Energy-moisture balance model (EMBM) calculated climatological surface air temperature. The contour interval is 2°C , with dashed contours indicating negative values. (b) Comparison of zonally averaged modeled surface air temperatures (solid) with the Comprehensive Ocean-Atmosphere Data Set (COADS) based observations (dashed-dotted) from *da Silva et al.* [1994a].

and ship bias. The present analysis utilizes the COADS-based wind speed estimates of *da Silva et al.* [1994b]. These estimates are converted from Beaufort winds and objectively analyzed to a $1^\circ \times 1^\circ$ grid. As we have mentioned, the gridding analysis introduces some amount of uncertainty; however, the Beaufort conversion also introduces some degree of uncertainty. Since we are incapable of estimating the uncertainty in these processes, we assume a 10% uncertainty as in the work of *Blanc* [1987]. Having explained our rationale for choosing parameters as they appear, we now consider the ability of the energy-moisture balance model to simulate present-day climatological conditions.

3. Model Results

3.1 Present Day Climatology

In a simple application of the energy-moisture balance model, we begin by considering the inferred atmospheric climatology when the SST is fixed to the annual *Levitus* [1982] surface climatology and the surface wind speed and solar insolation are fixed to the annual climatologies of *da Silva et al.* [1994b], and *Graves et al.* [1993], respectively. Figure 4 indicates the SST field we prescribe as the lower boundary condition for the atmospheric model, the landmass is shaded.

Figure 5a indicates our model-predicted surface air temperatures. Spatially, these patterns are quite real-

istic. The basin mean modeled surface air temperature over the ocean regions is 17.91°C for the climatological case, comparable to the basin mean value of 17.98°C based on the COADS analyzed data of *da Silva et al.* [1994a]. Figure 5b depicts a comparison of the zonally averaged data of *da Silva et al.* with our modeled fields (note that as COADS data exist only over the ocean regions, our fields are zonally averaged only over the ocean for comparison purposes). Clearly, the modeled fields are quite close to observations, with differences generally less than 0.5°C . It is interesting to note that the southern hemisphere temperatures (poleward of $65^{\circ} - 70^{\circ}$) are actually warmer than climatology, while the same region in the northern hemisphere is cooler. We attribute this effect to (1) the lower planetary emissivity in the southern regions as compared to northern polar regions and (2) the lower applied coalbedo in the northern hemisphere (Figure 2d).

Blanc [1987] indicates that because of ship and sensor error, rms errors of 0.6°C are not uncommon in ship-based estimates; hence the noted differences of roughly 0.5°C are not unreasonable. The generally lower surface air temperatures in the northern region of our model domain may simply be a consequence of neglecting the buffering effects of ice processes in our model. Alternatively, this may be due to (1) inefficient poleward transport of heat by the eddy diffusive approximation we employ, (2) the poleward heat transport implied by specifying the *Levitus* [1982] SST field, or (3) the generally low precipitation rate in the polar regions of our domain (see Figure 8b).

An exception to the generally cooler surface air temperatures occurs over the western boundary currents and in the subpolar gyres. We expect these deficiencies (in which T_{air} is up to 2°C higher than observations) to be primarily due to the absence of cold polar outbreaks (that may occur in a seasonally varying dynamical model) and the zonality of isotherms over the landmass in the present simulation (see Figure 5a).

The modeled specific humidity is depicted in Figure 6a (expressed in grams of water vapor per kilogram of moist air). As expected from the Clausius Clapeyron relation, the highest humidities are found in the equatorial zones and closely resemble the patterns of surface air temperature, as in the observations. Again, comparison with the COADS-based analysis of *da Silva et al.* [1994a] (see Figure 6b) indicates that our modeled specific humidity is quite close to observation, although generally about 0.5 g/kg higher than observations. The basin mean specific humidity over the oceans is 12.25 g/kg comparable to the COADS estimate of 11.81 g/kg . *Blanc* [1987] indicates the rms error of ship-based specific humidity measurement is roughly 0.2 g/kg , a little lower than the differences noted here.

As in the modeled surface air temperature fields, differences between the specific humidity fields of up to 2 g/kg exist in the subpolar gyre regions. These latter deficiencies are directly related to the higher model

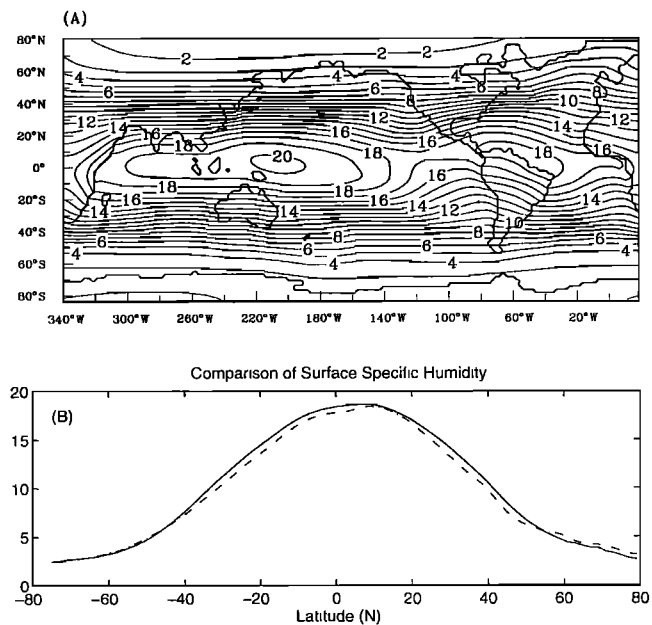


Figure 6. (a) EMBM-calculated climatological surface specific humidity. The contour interval is 1 g/kg . (b) Comparison of zonally averaged modeled specific humidity (solid) with COADS-based observations (dashed-dotted) from *da Silva et al.* [1994a].

surface air temperatures in the subpolar gyre regions. The overall higher specific humidities are also perhaps related to the precipitation parameterization employed here. From (12) and (13) we see that the model tends toward specific humidities close to 85% saturation. By comparison the observed specific humidity ranges from 70 to 85% saturated, indicating that our modeled values are roughly what one would expect under our atmospheric assumptions. Other minor differences between the modeled specific humidity and the observations occur near mountain ranges (which provide blocking of atmospheric water vapor transport and are not present in our model) and over the dry desert regions [cf. *Peixoto and Oort*, 1992, Figure 12.3a].

The modeled evaporation is depicted in Figure 7a and indicates that the highest evaporative rates occur over the midlatitude subtropical gyres. The maximum evaporation (in excess of 2.0 m/yr) occurs in the midlatitude North Atlantic, comparable to previous studies [e.g. *Baumgartner and Reichel*, 1975; *da Silva et al.*, 1994c]. The zonally averaged modeled evaporation is compared to the estimates of *da Silva et al.* in Figure 7b. It is evident that our modeled fluxes are generally lower than the observationally derived estimates by 0.2 m/yr .

Blanc [1985] applied 10 different formulations for the bulk transfer coefficients to the same set of ship observations. Subsequent analysis revealed average mean variations of 15–30% for the fluxes. The differences between our modeled fluxes and those of *da Silva et al.* [1994c] amount to roughly 20%, indicating we are

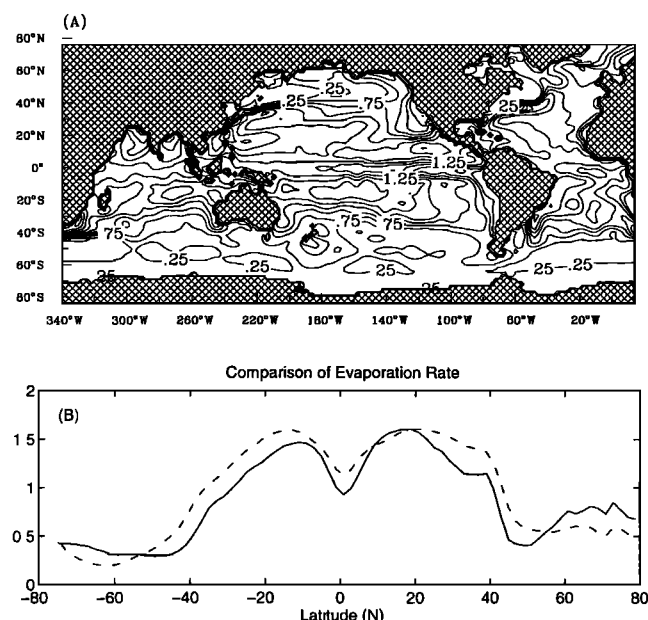


Figure 7. (a) EMBM-calculated climatological evaporation rate. The contour interval is 0.25 m/yr. (b) Comparison of zonally averaged modeled evaporation rate (solid) with COADS-based estimates (dashed-dotted) from *da Silva et al.* [1994c].

within the acceptable range due to the use of differing transfer coefficient formulations.

Figure 8a indicates the model-derived precipitation. In general, the highest precipitation rates (in excess of 1.5 m/yr) occur within the equatorial regime ($\pm 20^\circ$),

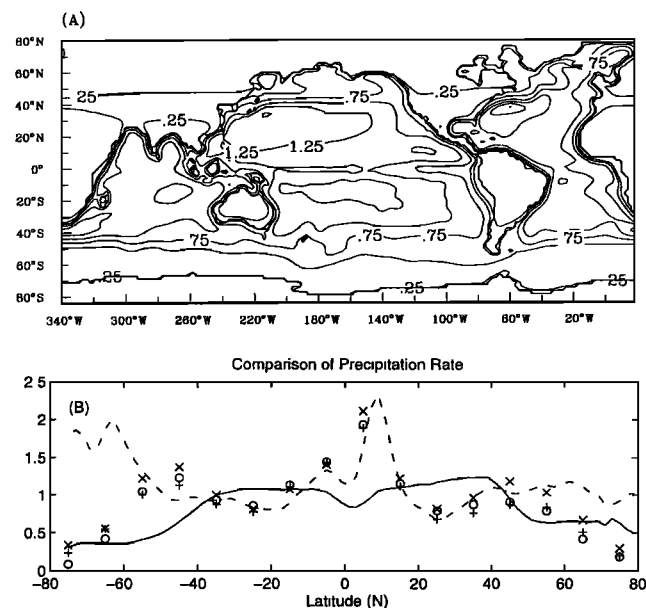


Figure 8. (a) EMBM-calculated climatological precipitation rate. The contour interval is 0.25 m/yr. (b) Comparison of zonally averaged modeled precipitation rate (solid) with COADS-based estimates (dashed-dotted) from *da Silva et al.* [1994c]. Also shown are the estimates of *Jaeger* [1983, crosses], *Sellers* [1965, circles], and *Baumgartner and Reichel* [1975, pluses].

while over much of Africa, central South America, and central Australia, the precipitation rate is negligible. Because of the rather crude diffusive transport mechanism we employ, our modeled precipitation fields are quite smooth. Nonetheless, spatially, our features agree with previous estimates. As in observations, a secondary maximum in our modeled precipitation fields exists over the northern subtropical North Atlantic. Toward the polar regions, the atmospheric moisture content is low, and precipitation rates reflect this with rates of less than 0.2 m/yr. The zonally averaged modeled precipitation rate is contrasted with the *da Silva et al.* [1994c] COADS-based estimates in Figure 8b. Unlike the evaporation rate, the magnitude of our precipitation rates appear quite poor when compared to observations. Although accurate measurements of precipitation are difficult to make (especially over the oceans), it is evident that not all the discrepancies of Figure 8b can be attributed to this effect. Our modeled field clearly fails to capture the high precipitation associated with strong convection in the intertropical convergence zone. The precipitation is therefore smeared over $\pm 40^\circ$ of the equator.

The model-derived freshwater flux (evaporation minus precipitation) is depicted in Figure 9a. The inadequacy of the modeled precipitation fields (especially in the ITCZ) is quite evident [cf. *Baumgartner and Reichel*, 1975; *Bryan and Oort*, 1984; *Schmitt et al.*, 1989; *da Silva et al.*, 1994c]. It is encouraging to note, however, that in the present simulation the North Atlantic evaporates 0.18 m/yr more water than is precipitated,

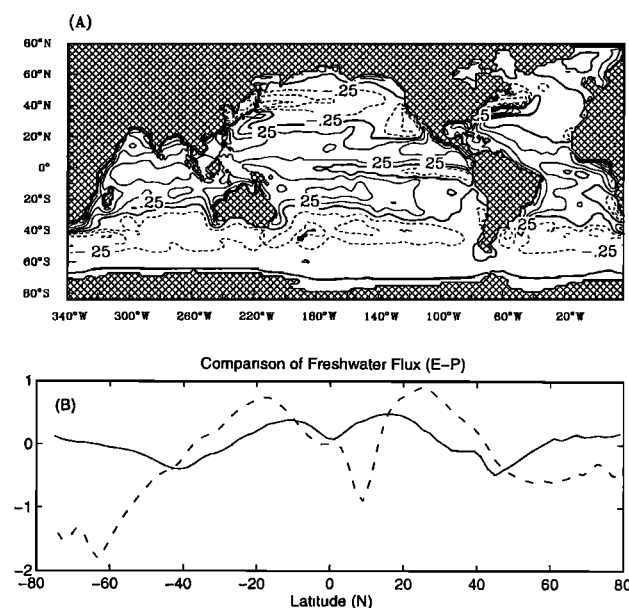


Figure 9. (a) EMBM-calculated climatological freshwater flux ($E - P$). The contour interval is 0.25 m/yr, with dashed contours indicating negative values. (b) Comparison of zonally averaged modeled freshwater flux (solid) with COADS-based estimates (dashed-dotted) from *da Silva et al.* [1994c].

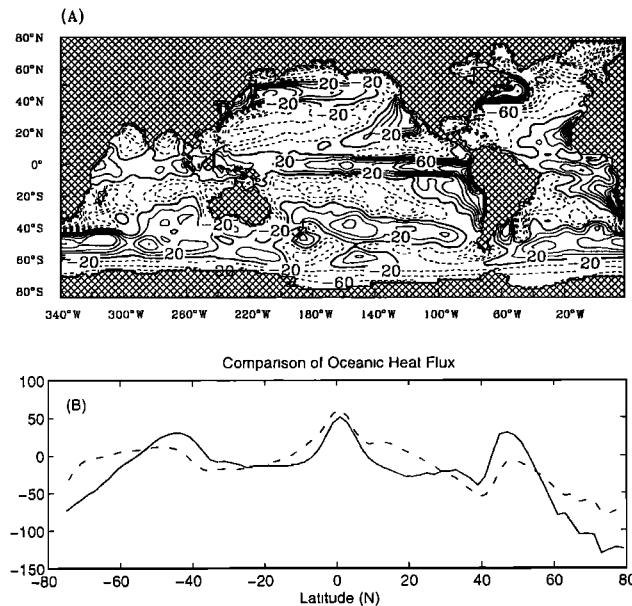


Figure 10. (a) EMBM-calculated climatological oceanic heat flux. The contour interval is 20 W/m², with dashed contours indicating heat flux out of the ocean. (b) Comparison of zonally averaged modeled oceanic heat flux (solid) with COADS-based estimates (dashed-dotted) from *da Silva et al.* [1994b].

comparable to the 0.26 m/yr inferred from *da Silva et al.* [1994c].

The model-predicted net heat flux into the ocean is presented in Figure 10a. In general, the results agree well with previous estimates [e.g., *Esbensen and Kushnir*, 1981; *Hsiung*, 1986; *Isemer et al.* 1989; *da Silva et al.*, 1994b] with a net heat gain at the equator and loss at the poles.

Over the warm subtropical gyres (e.g., the Gulf Stream and Kuroshio), net heat loss occurs, with the Gulf Stream having the largest loss, as in observations. As in observational data sets, net oceanic heat losses are clearly evident in the Leeuwin Current and Agulhas retroflection regions, while oceanic heat gains can be seen in the subpolar western boundary currents (e.g.,

the Labrador and Oyashio Currents), as well as within wind-driven upwelling fronts (e.g., the Benguela and Peru Currents). Comparison of plan views of our modeled heat fluxes with the *da Silva et al.* [1994b] analysis (not shown) indicates that while the general features agree, many of our features are too broad, indicating our diffusive transport should perhaps be supplemented by the vertically integrated advective heat transport by the atmosphere.

Figure 10b contrasts the modeled oceanic heat flux with that of *da Silva et al.* [1994b]. While the general features agree, our modeled fluxes are of the wrong sign within the latitude range $\sim 40^\circ - 60^\circ\text{N}$ (heat into the ocean). This effect is related to the generally higher surface air temperatures over the subpolar regions (see Figure 5a). Furthermore, the discrepancies poleward of 60° may be related to the absence of ice processes in the present model which would tend to buffer the ocean against such large heat losses. Finally, we note that the *da Silva et al.* [1994b] heat fluxes have been constrained by using observed oceanographic heat transports; hence some amount of the noted differences could be related to the corrections due to this process (see *da Silva et al.*, 1994d, Figure 8,9; *Isemer et al.*, 1989).

Considering the discrepancies between modeled and observed oceanic heat fluxes of Figure 10a, it is not surprising that the implied oceanic heat transport (not shown) is not very realistic. Errors of this magnitude lead to a fictitious heat transport (because of error accumulation during integration) of several petawatts [*Peuróto and Oort*, 1992]. This is not the case in section 5 where we couple a global ocean general circulation model to the energy-moisture balance model.

3.2. Sensitivity to Model Parameters

In an effort to assess the sensitivity of the present climatology to our choice of model parameters, a series of experiments were performed in which each parameter was independently varied between $\pm 40\%$ of their derived values.

The present definition of sensitivity differs slightly from its traditional meaning when applied to energy

Table 2. Summary of Model Sensitivity Experiments

Parameter	Symbol	T_G °C	T_E °C	Q_G g/kg	Uncertainty %
$(1 - \alpha)$	solid	0.08	0.07	0.04	5
C_0	crosses	-0.08	-0.07	-0.04	10
ε_P	dashed	-0.12	-0.10	-0.06	5
ε_A	dotted	-0.08	-0.09	-0.05	4.4
T_{sea}	dashed-dotted	0.18	0.25	0.16	.033
U	circles	0.02	0.02	0.02	10

Column 1 indicates model parameter varied; column 2, the plotting legend (see Figure 11); columns 3-5 indicate the global temperature, equatorial temperature, and global specific humidity changes for a 1% change in model parameter. Column 5 indicates the estimated uncertainty in model parameters (see section 2.3).

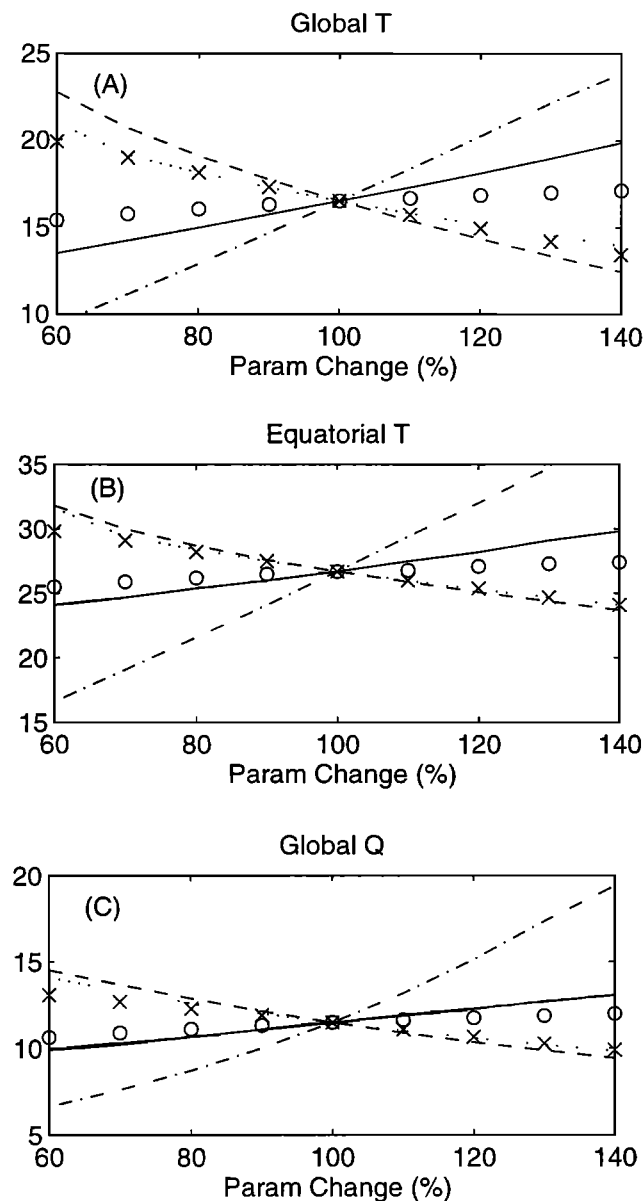


Figure 11. Summary of the model parameter sensitivity study. Graphs indicate the change in modeled (a) global surface air temperature, (b) global specific humidity, (c) equatorial surface air temperature, due to a percentage increase in each model parameter (see also Table 2).

balance models. In the present application the ocean state essentially remains fixed, so that a rather strong constraint is implicitly imposed on the modeled climate.

The results of our sensitivity experiments are summarized in Table 2 (columns 3-5 indicate the change in temperature and specific humidity due to a 1% change in model parameter, column 1 as derived from Figure 11). The greatest model sensitivities arise from parameters affecting the net boundary fluxes: the SST (T_{sea}) and planetary emissivity (ϵ_P). Note, however, that within the context of the estimated uncertainty in model parameters (tabulated in column 6, Table 2) the

largest change in equatorial temperature (T_E) (Figure 11c) is only roughly 0.7°C , essentially the uncertainty in ship based estimates [Blanc, 1987].

If we consider increasing (decreasing) all parameters to their maximum (minimum) uncertainty values (see Table 2), the equatorial air temperature changes by roughly 0.5°C (0.1°C). This effect is attributed to the competing effects of the model air temperature sensitivity as in Figure 11a.

These results suggest that within the limits of the estimated uncertainty in our model parameters, the modeled climatology is quite robust. This analysis is far from conclusive, however, since the ocean state is incapable of adjusting to the changes we describe.

4. Interannual Variability

4.1. Interpentadal Differences

In an effort to investigate our model changes due to changes in the ocean state, we now consider the atmospheric change obtained by prescribing the pentadal SST fields for 1955-1959, and 1970-1974 [Levitus, 1989]. While systematic model deficiencies are evident in the model climatology, the argument here is that the climatology serves only as a reference state. The response of the system about this reference state is then assumed to be unaffected by the exact nature of the climatology [Sausen et al., 1988; Cubasch et al., 1992].

Figure 12a indicates the interpentadal surface air temperature difference (1955-1959 minus 1970-1974)

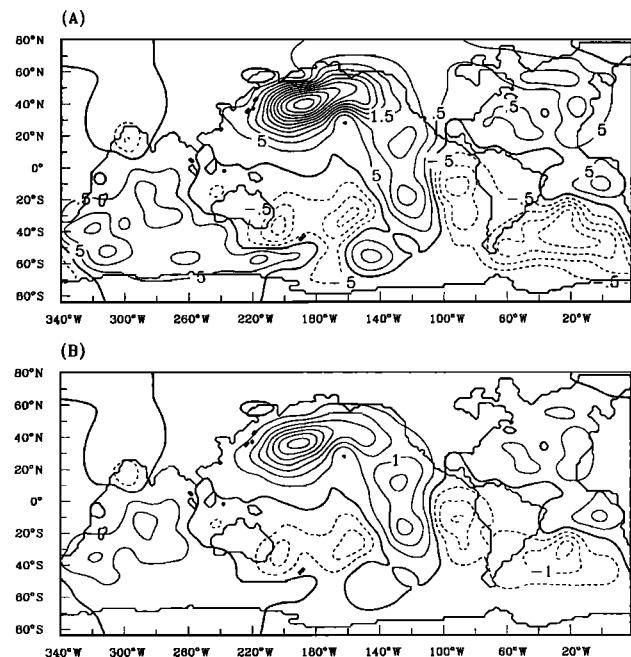


Figure 12. (a) EMBM-calculated interpentadal surface air temperature, (1955-1959 minus 1970-1974). The contour interval is 0.5°C , with dashed contours indicating negative values. (b) As in Figure 12a, but for specific humidity. The contour interval is 0.5 g/kg .

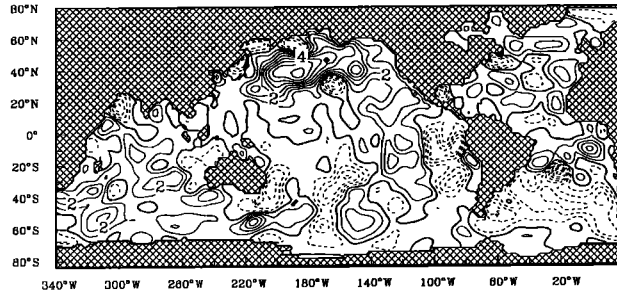


Figure 13. Interpentadal SST (1955-1959 minus 1970-1974). The contour interval is 1.0°C , with dashed contours indicating lower values in the 1955-1959 pentad.

predicted by our energy-moisture balance model. By comparison with Figure 13, we see that the model-predicted surface air temperature difference is essentially a forced local response to the imposed SST differences, smoothed by both sensible and latent heat diffusion. This can be seen if we neglect both moisture and diffusion effects in (2a) and linearize the gray body approximations (as in (5b)). The resulting expression is almost a one-to-one linear response between the SST and the air temperature anomalies. The main nonlinearity in the atmospheric model arises through terms involving the specific humidity which appear secondary in importance in the present application.

In general, the northern hemisphere is cooler in the pentad of the 1970s with the southern hemisphere warmer, the exception being the Indian Ocean which shows cooling comparable to the North Pacific. *Kawamura* [1994] noted a teleconnection in which anomalies over the central Pacific are closely linked to those over the Indian Ocean. The imposed SST anomalies reflect this, and our model responds directly to the imposed forcing.

The most dramatic model air temperature differences occur over the North Pacific, with a basin mean temperature of 1.17°C cooler during the 1970s. In the region $30^{\circ} - 40^{\circ}\text{N}$, $160^{\circ} - 180^{\circ}\text{E}$, the 1970s were up to 6°C cooler than the 1950s. This is perhaps related to a deepening of the Aleutian low (by several millibar) in the 1970s as compared to the 1950s. *Trenberth* [1990] and *Trenberth and Hurrell* [1994] indicate that a stronger Aleutian low is conducive to anomalously stronger winds, favoring colder than normal atmospheric conditions over the central and eastern Pacific. Such atmospheric conditions will then favor colder than normal SST anomalies in the central and eastern Pacific due to increased surface heat loss and ocean mixing during the 1970s pentad. Obviously, since our model contains no dynamics, the effects of the change in the Aleutian low are felt only through the changes in the prescribed pentadal SST fields.

The Indian Ocean also indicates a basin mean temperature of 0.59°C cooler during the 1970s with temperatures up to 3°C lower. Similarly, the North Atlantic indicates roughly 0.39°C lower temperatures (during

the 1970s), with a minimum of 1.5°C occurring in the Labrador Sea and south of Greenland. This is associated with the occurrence of the "Great Salinity Anomaly" during the 1970s [*Dickson et al.*, 1988]. Our results also indicate warming (in the 1970s) throughout the South Atlantic of 0.71°C , with maxima of up to $2^{\circ} - 3^{\circ}\text{C}$, while the South Pacific shows warming of roughly 0.22°C . Unfortunately, because of the paucity of data in the Southern Ocean, it is difficult to ascertain whether these latter results are observed in the climate record.

As is to be expected from the Clausius Clapeyron relation, the lower northern temperatures (in the 1970s pentad) also result in a decreased ability for the atmosphere to hold moisture. Figure 12b indicates the model interpentadal specific humidity field, (1955-1959 minus 1970-1974). As in our climatological fields, the increases and decreases in specific humidity closely resemble the temperature differences of Figure 12a. The thermal control of the hydrological cycle is evident with decreased North Pacific, North Atlantic, and Indian Ocean specific humidities (during the 1970s) of 0.80 g/kg , 0.25 g/kg and 0.38 g/kg , respectively. Correspondingly, the South Atlantic and South Pacific exhibit increases (during the 1970s pentad) of 0.29 g/kg and 0.16 g/kg , respectively. Similar effects are also noted in the model-derived precipitation and evaporation (see Table 3).

The globally averaged surface air temperature is found to be some 0.27°C cooler during the 1970s pentad, comparable to estimates of *Jones et al.* [1986a, b], *Hansen and Lebedeff* [1987], *Jones* [1988]. As well, the northern hemisphere cooling into the 1970s and warming in the southern hemisphere are consistent with the data of *Jones et al.* [1986a, b], *Jones* [1988], and *Wigley and Barnett* [1990].

Although it is difficult to compare our modeled temperature change (forced by oceanic changes) to that inferred by *Hansen and Lebedeff* [1987] (who considered primarily land-based observations), the model results are comparable to their data when averaged over the same pentads. In fact, our eastern Canadian and eastern United States air temperatures show decreases (in the 1970s versus 1950s pentad) of 0.42°C and 0.34°C , comparable to *Hansen and Lebedeff's* estimates of 0.78°C and 0.23°C , respectively. The agreement is

Table 3. Basin Mean, Model-Calculated, Interpentadal (1955-1959 minus 1970-1974) Fields

Basin	$T^{\circ}\text{C}$	$Q\text{g/kg}$	$P\text{m/yr}$	$E\text{m/yr}$
Indian	0.59	0.38	0.029	0.036
North Pacific	1.17	0.80	0.052	0.067
North Atlantic	0.39	0.25	0.019	0.015
South Pacific	-0.22	-0.16	-0.019	-0.030
South Atlantic	-0.71	-0.29	-0.023	-0.029
Global	0.27	0.20	0.011	-0.011

less good for western Canada and the western United States which exhibit decreases (in the 1970s versus the 1950s pentad) of 0.60°C and 0.84°C , respectively, while Hansen and Lebedeff indicate increases of 0.06°C and 0.21°C . Similarly, over eastern and central Europe our modeled fields indicate temperature changes of -0.04°C and 0.41°C , whereas the Hansen and Lebedeff data indicate changes of -0.21°C and -0.36°C (i.e., warming in the 1970s versus the 1950s pentad).

As noted, the global temperature change of roughly 0.3°C is driven by the equivalent change in *Levitus* [1989] objectively analyzed SST fields. Clearly, one must be cautious in interpreting our results since the objective analysis procedure applied to the SST data could smear data from one station over a larger area. Such an effect, together with the smoothing nature of our diffusive atmosphere, could then misrepresent such a feature as "real". Analysis of the *Levitus* [1989] SST differences indicates that while many of the features are basin scale, some features have length scales consistent with the *Levitus* [1982] objective analysis length scale (see Figure 13). It is encouraging to note that the atmospheric features described above are of basin scale, indicating the ability of our model to dampen such small-scale features. We therefore believe that while a point-by-point comparison with direct observations is inappropriate, the basin and global statistics are significant, at least within the context of the basin and global scale significance of the *Levitus* [1989] SST.

4.2. Sensitivity to Model Climatology

In computing the interpentadal fields (1955-1959 minus 1970-1974), we have implicitly assumed that systematic model biases are merely an artifact of the background climatology and do not affect the atmospheric response to a perturbation about the reference state. [Sausen *et al.*, 1988; Cubasch *et al.*, 1992].

As a test of the robustness of our interpentadal results, we adjust our model parameters to yield a completely unacceptable climatology, as well as a climatology that is marginally acceptable. This is accomplished by increasing the planetary emissivity and decreasing the atmospheric emissivity and amount of solar radiation absorbed by the atmosphere.

In the first test, the climatology is adjusted so that air temperatures are consistently 1°C colder than our original climatology over the ocean basin and up to 9°C colder over central Europe (we term this the marginally acceptable case; see Figure 14a). The corresponding interpentadal temperature and specific humidity fields are depicted in Figures 14b and 14c and are virtually indistinguishable from the interpentadal fields of Figures 12a and 12b. In fact, the globally averaged temperature has changed by less than 0.02°C , with the largest change (of 0.04°C) occurring over the North Pacific.

In an additional test, the modeled climatology is adjusted so that the surface air temperatures are consis-

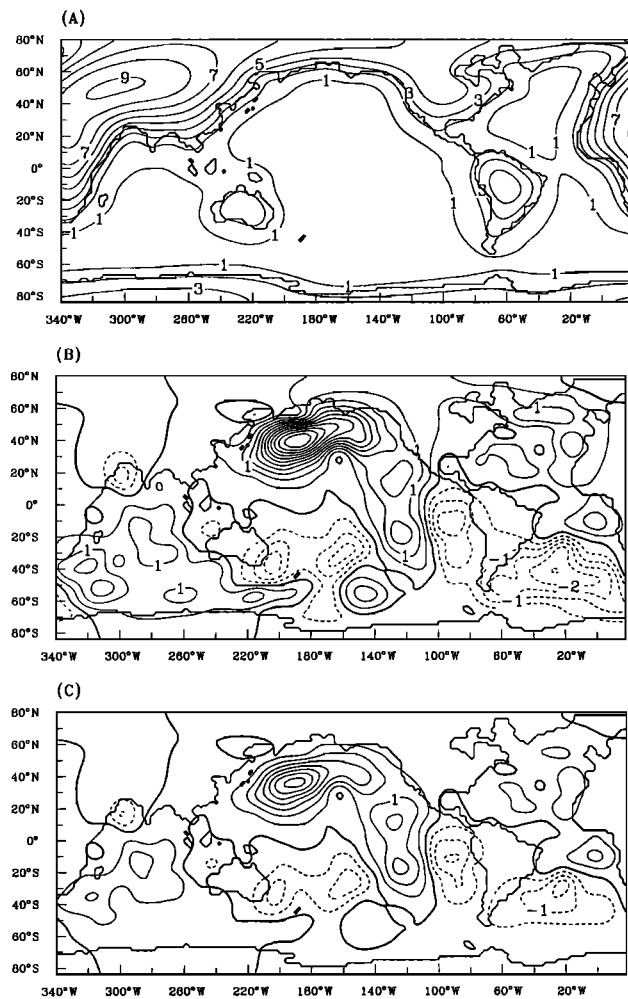


Figure 14. (a) Difference of marginally acceptable model climatology from that of Figure 5a. (b) As in Figure 12a but for the marginally acceptable climatology case. (c) As in Figure 14b but for specific humidity.

tently 4°C cooler than our original climatology over the ocean basin and up to 29°C cooler over central Europe (the unacceptable climatology case; see Figure 15a). Again, the interpentadal fields (see Figure 15b and 15c) are indistinguishable from those produced from our original climatology's parameters. Here the global air temperature difference is less than 0.03°C , with the largest change again occurring over the North Pacific (0.09°C).

The interpentadal modeled differences are quite robust, changing remarkably little even though the background state has changed dramatically. Again, by comparison with Figure 13 we see that the model-predicted surface air temperature difference is essentially a forced local response to the imposed SST differences. This is again related to the almost perfect linear relation between SST and air temperature anomalies, with diffusion of sensible and latent heat acting to smooth the field.

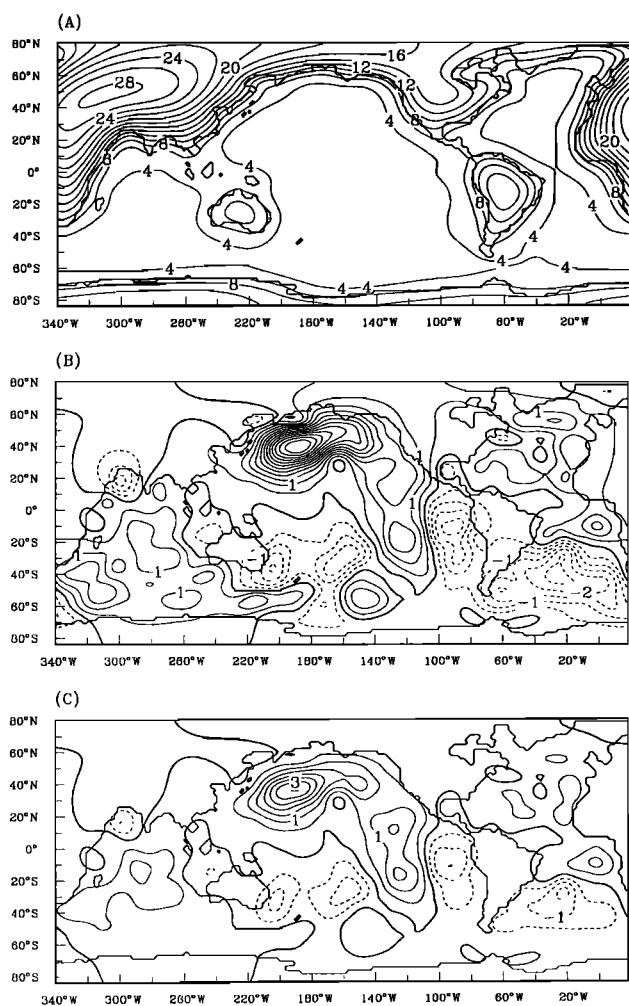


Figure 15. (a) Difference of unrealistic model climatology from that of Figure 5a. (b) As in Figure 12a but for the unrealistic climatology case. (c) As in Figure 15b but for specific humidity.

5. Coupled Ocean-Atmosphere Results

We now relax the constraint of fixed oceanic state by coupling the energy-moisture balance model to a global, realistic geometry version of the Geophysical Fluid Dynamics Laboratory-Modular Ocean Model (GFDL MOM) model (Pacanowski, *et al.* [1993]; see Weaver and Hughes, [1996] for full details of the OGCM). The model is of 3.75° zonal resolution, 1.8555° meridional resolution, and contains 19 levels in the vertical. Precipitation over the landmass is instantaneously returned to the ocean by a series of river drainage basins [see Weaver and Hughes, 1996, Figure 6]. To allow for the buffering effects of ice (as well as the ice-albedo feedback), we incorporate a simple thermodynamic ice model [Semtner, 1976] which allows for brine rejection during growth, as well as heat insulation. Ice albedo effects over land are incorporated by assuming that ice/snow exists if the land temperature drops below -10°C . We also allow for the water-vapor planetary

longwave feedback by replacing our planetary gray body approximation (5a) by the empirical formula of Thompson and Warren [1982]. The coupled EMBM-OGCM integration begins from the equilibrium ocean climate of Weaver and Hughes [1996] (obtained after a 4000-year integration under restoring boundary conditions), to which the atmospheric model (beginning from zero heat and moisture content) is coupled. The coupled system is then integrated an additional 1000 years, at which time the basin mean heat flux has dropped below 10^{-2} W/m^2 .

The zonally integrated meridional overturning streamfunction indicates the strength of the thermohaline circulation (Figures 16a, 16b, and 16c for the Atlantic, Pacific plus Indian, and global oceans, respectively). The interbasin-scale thermohaline circulation [Broecker, 1991] is evident with roughly 20 Sverdrups (Sv) of North Atlantic deep water forming, 11 Sv of which is ex-

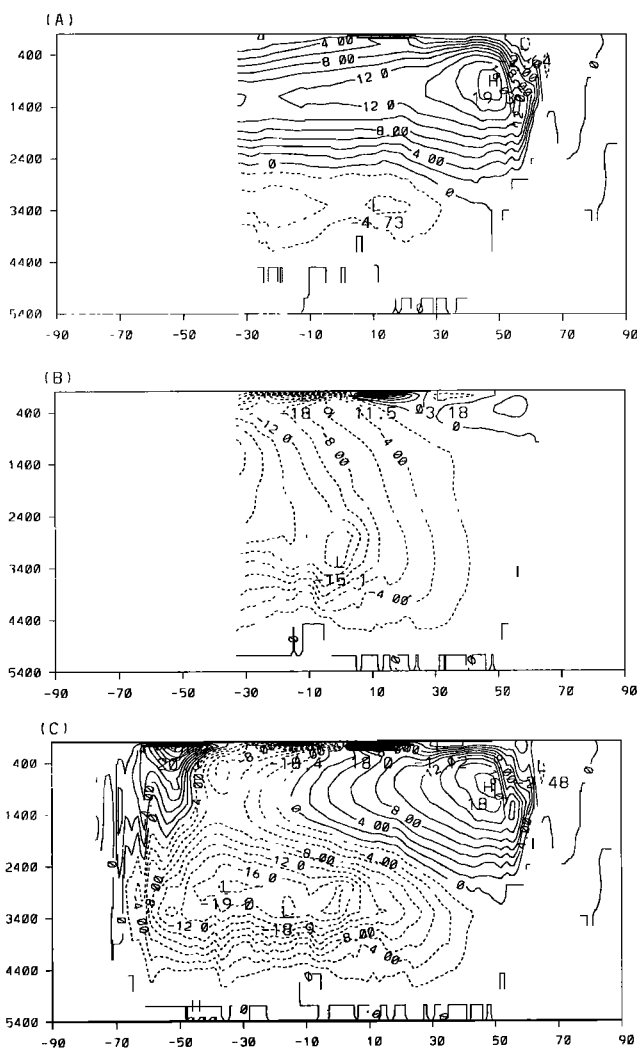


Figure 16. (a) Mean meridional overturning streamfunction in the Atlantic basin. (b) as in Figure 16a but for the Pacific and Indian basins combined. (c) As in Figure 16a but for the global basin. The contour interval is 2 Sv, 1 Sv = $10^6 \text{ m}^3/\text{s}$.

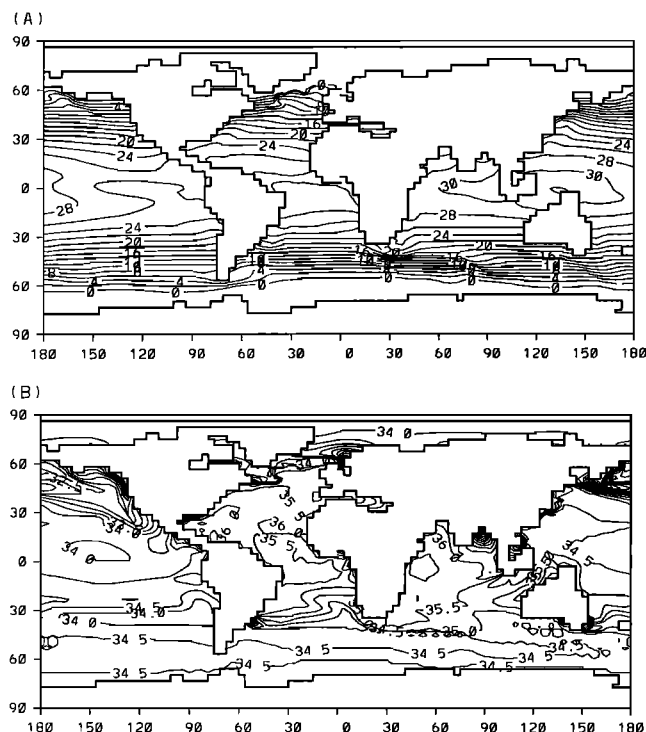


Figure 17. (a) Model-simulated SST. The contour interval is 2°C. (b) Model-simulated SSS. The contour interval is 0.5 psu (practical salinity units).

ported to the Southern Oceans (cf. 14 Sv inferred by Schmitz [1995]). Below the North Atlantic cell, roughly 4 Sv of Antarctic Bottom Water (formed in the Weddell and Ross Seas) fills the abyss; this also agrees well with the 2–4 Sv estimate of McCartney [1992]. The North Pacific and Indian Oceans are regions of broad upwelling, which is reproduced by our coupled model (see Figure 16b). It is common for equilibrium coupled ocean-atmosphere model simulations (without flux adjustments) to form deep water in the Pacific and not in the other basins. Hence the absence of North Pacific deep water in our model is a powerful result, especially in light of the fact that no flux corrections are employed. In Figure 16c we show the globally averaged overturning streamfunction which illustrates the competing effects of the North Atlantic versus Antarctic overturning cells, also evident is the Deacon cell in the Southern Ocean [Döös and Webb, 1994].

Comparing Figure 17a with Figure 5, the modeled SST is quite close to climatology. Because of our use of a clear sky albedo the equatorial surface temperatures are roughly 1°C too warm, while the polar temperatures are too cool, and hence our ice line (not shown) extends too far south. Figure 17b indicates the modeled surface salinity. Even though the modeled precipitation fields are diffuse, Figure 17b indicates that our model captures the salient features of the SSS, although some regions are arguably too fresh (e.g., the Norwegian Sea; cf. Levitus, [1982], Figure 22). The midlatitude North

Atlantic is roughly 2 psu (practical salinity units) saltier than the Pacific, and the northern Pacific shows a strong halocline which inhibits deep water formation there.

The zonal mean potential temperature distributions for the global as well as the Atlantic oceans are shown in Figure 18, and are comparable to direct observations (cf. Levitus, [1982], Figure 98 and 110). Most OGCMs (when run under restoring boundary conditions) exhibit a warm deep ocean bias (of 2°–4°C) and a diffuse thermocline. Providing for a more realistic surface heat flux parameterization, the warm bias is reduced significantly in the present model (cf. Figure 18 with Weaver and Hughes, [1996], Figure 5). Even though the thermocline is still a bit too diffuse, it is in much better agreement with observations. Figure 19 illustrates the zonal mean salinity distribution for the Atlantic Ocean, which is also comparable to direct observations (cf. Levitus, [1982], Figure 111). Several water mass signatures are evident in Figure 19; the saline Mediterranean waters (included in the coupled model) [see Weaver and Hughes, 1996] are evident at roughly 35°N; we also note the distinct signatures of the warm

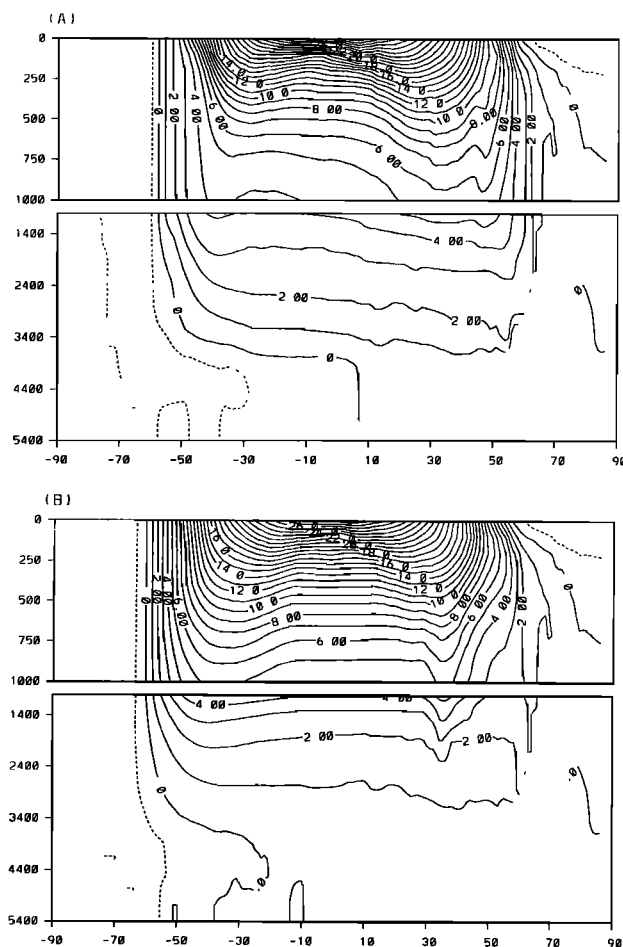


Figure 18. (a) Annual mean Atlantic zonally averaged potential temperature. The contour interval is 1°C; dashed contours indicate negative values. (b) as in Figure 18a but for the global ocean.

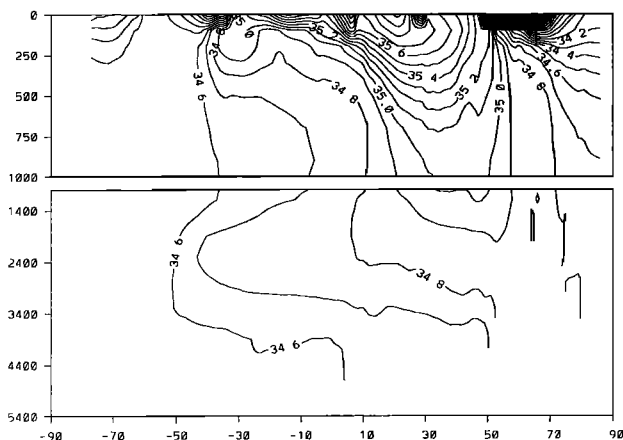


Figure 19. Annual mean Atlantic zonally averaged salinity. The contour interval is 0.1 psu.

saline North Atlantic deep water overriding the cold, less saline Antarctic Bottom Water and spreading beneath the fresher Antarctic Intermediate Water.

The planetary poleward heat transport in the coupled ocean-atmosphere model is depicted in Figure 20a. The planetary heat transport is poleward in each hemisphere, with roughly 6.2 PW (1 PW = 10^{15} W) at 30° N and -7 PW at 35° S. Compared with observational estimates, the planetary heat transport is roughly 20% too high but may be within the observational errors [Peiróto and Oort, 1992] especially since a few watts per meter squared integrated over large areas cause large changes in the poleward heat transport. The poleward heat transport within the model Atlantic and Global ocean are illustrated in Figure 20b. Heat is transported northward everywhere in the Atlantic, with a maximum of over 0.7 PW between the equator and 30° N. This is an increase of ~ 0.2 PW over the same ocean model when driven under restoring boundary conditions and reflects the better representation of surface to deep water temperature contrast in the coupled model. The global ocean heat transport, Figure 20b, reveals a maximum transport slightly more than half that derived from observational estimates, a persistent problem in coarse resolution ocean models. Because the planetary heat transport is too high and the oceanic heat transport is too low, it is not surprising that the atmospheric heat transport is also too high (Figure 20a) to compensate.

6. Summary and Conclusions

An atmospheric model incorporating energy and moisture balance equations has been developed for use in process studies of the coupled ocean-atmosphere system. Physically, the thermodynamic branch of our model is similar to the earlier energy balance models of Budyko [1969], Sellers [1969], and North [1975a] to which we have added forcing terms arising from the

air-sea interaction. The hydrological cycle is modeled by employing an eddy-diffusive approximation to the atmospheric moisture balance equation. A traditional bulk formula expresses the source term from evaporation, while the precipitation is parameterized in terms of the atmospheric specific humidity.

Under fixed climatological SST and wind speed the model surface air temperatures, specific humidities, evaporation, and oceanic heat flux are comparable to observations. Unfortunately, because of the simplicity in the parameterizations we employ, as well as systematic biases in the model formulation, our modeled climatology does exhibit inconsistencies when compared to previous works. In particular, (as noted in section 3.1) the polar heat fluxes are too large, perhaps because of the absence of the buffering effect of sea ice. The zonality of isotherms over the land may be rectified by appealing to a simplified land process model (as in the work of Manabe and Stouffer, [1988]), or the inclusion of topography and advection effects in the heat and moisture balance equations. The limitations of our eddy-diffusive transport mechanism is also evident in the rather smoothed and broad features of our modeled heat fluxes and precipitation (which fails to capture the strong ITCZ precipitation signal).

As an extension to the fixed climatological experiment, a simple perturbation experiment in which the 1955-1959 pentad is compared to the 1970-1974 pentad is conducted. The North Pacific, North Atlantic and Indian Ocean basins show surface air temperature decreases in the 1970-1974 pentad of 1.17°C , 0.39°C and 0.59°C , respectively, while the South Atlantic and South Pacific exhibit increases of 0.71°C and 0.22°C respectively. The thermal control of the ocean/air temperatures on the hydrological cycle is also evident

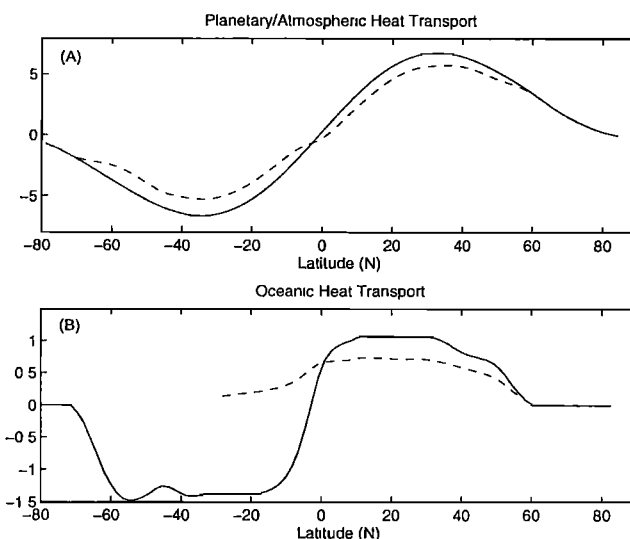


Figure 20. (a) Planetary (solid) and atmospheric (dashed) heat transport in the coupled model. Units are in PW ($1\text{PW} = 10^{15}\text{W}$). (b) As in Figure 20a but for the Atlantic (dashed) and global (solid) oceans.

with decreased North Pacific, North Atlantic and Indian Ocean specific humidities of 0.80 g/kg, 0.25 g/kg and 0.38 g/kg, respectively (during the 1970-1974 pentad). Correspondingly, the South Atlantic and South Pacific exhibit increases of 0.29 g/kg and 0.16 g/kg, respectively. Similar effects are also noted in the model-derived precipitation and evaporation.

Comparing the model-predicted surface air temperature differences to the interpentadal SST differences, the atmospheric response is essentially a forced local response to the imposed SST differences, smoothed by both sensible and latent heat diffusion. The model results change remarkably little even when parameters representing completely different climatological states are employed. This can be understood in light of the almost linear relation between SST and air temperature anomalies in our idealized model.

The modeled global temperature decrease in the latter pentad of 0.27°C is comparable to the direct estimates of Jones *et al.* [1986a, b] and Jones [1988]. Analysis of the Levitus [1989] sea surface temperature differences indicates that while many of the features are basin scale, some features have length scales consistent with the Levitus [1982] objective analysis length scale. This compounds the problem of attaching significance to our results. The atmospheric features we describe are of basin scale, however, indicating the ability of our model to smooth out such small-scale features. We therefore believe that the interpentadal basin and global statistics we have diagnosed are significant (at least within the context of the significance of the Levitus [1989] SST differences).

Relaxing the constraint of fixed oceanic state, the coupled EMBM-OGCM faithfully reproduces the present-day climate, without the need for flux corrections. The global thermohaline circulation is well represented, with no deep water formation occurring in the North Pacific. Although the model precipitation fields are generally too diffuse, the model SSS fields agree reasonably well with observations. Our results also suggest a great improvement in water characteristics when the model is coupled, with elimination of the deep warm temperature bias and shallowing of the generally diffuse modeled thermocline, features prevalent in many ocean-only simulations. Global atmospheric and planetary heat transports are quite close to observational estimates, although roughly 20% too high, while the global oceanic heat transport is slightly more than half that expected from observational estimates.

The energy-moisture balance model's strength lies in its simplicity. The model relates all components of the atmospheric system to only three variables: surface air temperature, SST and specific humidity. In this manner the model includes the primary hydrological and thermodynamic processes within the climate system, yet utilizes only modest computer resources.

Although systematic model deficiencies exist, we believe the model should be useful for coupled ocean-

atmosphere studies on climate timescales. Of particular interest is whether decadal timescale variability found in ocean-only models [e.g., Weaver and Sarachik, 1991; Weaver *et al.*, 1991, 1994; Weisse *et al.*, 1994; Greatbatch and Zhang, 1995] survives in our coupled model. If so, what are the mechanisms which sustain them? Furthermore, we wish to examine whether or not the "flush/collapse" of the thermohaline circulation [e.g., Marotzke 1989; Weaver and Sarachik, 1991; Zhang *et al.*, 1993] can exist when an atmosphere with finite heat capacity and heat and moisture feedbacks is coupled to an ocean model.

Acknowledgments. This research was funded through an Atlantic Career Development Award awarded to AFF, and operating grants awarded to AJW from NSERC/WOCE, NSERC, AES, CICS, DFO, and the NOAA Scripps-Lamont Consortium on the Ocean's Role in Climate. We are very grateful to Arlindo da Silva for supplying his analyzed fields, and for his numerous comments during model development, to T.M.C. Hughes for her enlightening comments on an earlier version of this manuscript, to Greg Flato for assistance in implementing the thermodynamic ice model, as well as to three anonymous reviewers for their helpful comments.

References

- Baumgartner, A., and E. Reichel, *The World Water Balance*, 179 pp., Elsevier, New York, 1975.
- Blanc, T.V., Variation of bulk-derived surface flux, stability and roughness results due to the use of different transfer coefficient schemes, *J. Phys. Oceanogr.*, **15**, 650-659, 1985.
- Blanc, T.V., Accuracy of bulk-method-determined flux, stability, and sea surface roughness, *J. Geophys. Res.*, **92**, 3867-3876, 1987.
- Bolton, D., The computation of equivalent potential temperature, *Mon. Weather Rev.*, **108**, 1046-1053, 1980.
- Bryan, F., and A. Oort, Seasonal variation of the global water balance based on aerological data, *J. Geophys. Res.*, **89**, 11,717-11,730, 1984.
- Broecker, W.S., The great ocean conveyor, *Oceanography*, **4**, 79-89, 1991.
- Budyko, M.I., The effect of solar radiation variations on the climate of the earth, *Tellus*, **21**, 611-619, 1969.
- Campbell, G.G., and T.H. Vonder Haar, Climatology of radiation budget measurements from satellites, *Atmos. Sci. Pap.* **323**, 74 pp., Dep. Atmos. Sci., Colo. State Univ., Boulder, 1980.
- Cubasch, U., K. Hasselmann, H. Höck, E. Maier-Reimer, U. Mikolajewicz, B.D. Santer, and R. Sausen, Time-dependent greenhouse warming computations with a coupled ocean-atmosphere model, *Clim. Dyn.*, **8**, 55-69, 1992.
- da Silva, A. M., C. C. Young, and S. Levitus, Anomalies of directly observed quantities, in *Atlas of surface marine data 1994*, vol. 2, 416 pp., Natl. Oceanic and Atmos. Admin., Washington, D.C., 1994a.
- da Silva, A. M., C. C. Young, and S. Levitus, Anomalies of heat and momentum fluxes, in *Atlas of surface marine data 1994*, vol. 3, 413 pp., Natl. Oceanic and Atmos. Admin., Washington, D.C., 1994b.
- da Silva, A. M., C. C. Young, and S. Levitus, Anomalies of freshwater fluxes, in *Atlas of surface marine data 1994*, vol. 4, 308 pp., Natl. Oceanic and Atmos. Admin., Washington, D.C., 1994c.
- da Silva, A. M., C. C. Young, and S. Levitus, Algorithms

- and Procedures, in *Atlas of surface marine data 1994*, vol. 1, 83 pp., Natl. Oceanic and Atmos. Admin., Washington, D.C., 1994d.
- Dickson, R.R., J. Meincke, S.A. Malmberg, and A.J. Lee, The "Great Salinity Anomaly" in the northern North Atlantic 1968-1982, *Prog. Oceanogr.*, **20**, 103-151, 1988.
- Döös, K., and D.J. Webb, The Deacon Cell and other meridional cells in the Southern Ocean, *J. Phys. Oceanogr.*, **24**, 429-442, 1994.
- Esbensen, S.K., and Y. Kushnir, The heat budget of the global ocean: An atlas based on estimates from surface marine observations, *Clim. Res. Inst., Rep. 29*, 124pp., Dep. Atmos. Sci., Oregon State Univ., Oregon, 1981.
- Fung, I.Y., D.E. Harrison, and A.A. Lacis, On the variability of the net longwave radiation at the ocean surface, *Rev. Geophys.*, **22**, 177-193, 1984.
- Gill, A.E., *Atmosphere-Ocean Dynamics*, 662 pp., Academic, New York, 1982.
- Graves, C.E., W.H. Lee, and G.R. North, New parameterizations and sensitivities for simple climate models, *J. Geophys. Res.*, **98**, 5025-5036, 1993.
- Greatbatch, R.J., and S.Z. Zhang, An interdecadal oscillation in an idealized ocean forced by constant heat flux, *J. Clim.*, **8**, 81-91, 1995.
- Haney, R.L., Surface thermal boundary condition for ocean circulation models, *J. Phys. Oceanogr.*, **1**, 241-248, 1971.
- Hansen, J., and S. Lebedeff, Global trends of measured surface air temperature, *J. Geophys. Res.*, **92**, 13,345-13,372, 1987.
- Hsiung, J., Mean surface energy fluxes over the global ocean, *J. Geophys. Res.*, **91**, 10,585-10,606, 1986.
- Huang, R., Real freshwater flux as a natural boundary condition for the salinity balance and thermohaline circulation forced by evaporation and precipitation, *J. Phys. Oceanogr.*, **23**, 2428-2446, 1993.
- Hughes, T.M.C., and A.J. Weaver, Sea surface temperature-evaporation feedback and the ocean's thermohaline circulation, *J. Phys. Oceanogr.*, **26**, 644-654, 1996.
- Isemer, H.J., J. Willebrand, and L. Hasse, Fine adjustment of large scale air-sea energy flux parameterizations by direct estimates of ocean heat transport, *J. Clim.*, **2**, 1173-1184, 1989.
- Jaeger, L., Monthly and areal patterns of mean global precipitation, in *Variations in the Global Water Budget*, edited by A. Street-Perrott et al., 129-146 pp., D. Reidel, Norwell, Mass., 1983.
- Jones, P.D. Hemispheric surface air temperature variations: Recent trends and an update to 1987, *J. Clim.*, **1**, 654-660, 1988.
- Jones, P.D., S.C.B. Rapier, and T.M.L. Wigley, Southern Hemisphere surface air temperature variations: 1851-1984, *J. Clim. Appl. Meteorol.*, **25**, 1213-1230, 1986a.
- Jones, P.D., R.S. Bradley, H.F. Diaz, P.M. Kelly, and T.M.L. Wigley, Northern Hemisphere surface air temperature variations: 1851-1984, *J. Clim. Appl. Meteorol.*, **25**, 161-179, 1986b.
- Kawamura, R., A rotated EOF analysis of global sea surface temperature variability with interannual and interdecadal scales, *J. Phys. Oceanogr.*, **24**, 707-715, 1994.
- Large, W.G., and S. Pond, Sensible and latent flux measurements over the ocean, *J. Phys. Oceanogr.*, **12**, 464-482, 1982.
- Levitus, S., Climatological atlas of the world ocean, *NOAA Prof. Pap.*, **13**, 177 pp., Natl. Oceanic and Atmos. Admin., Washington, D.C., 1982.
- Levitus, S., Interpentadal variability of temperature and salinity at intermediate depths of the North Atlantic Ocean, 1970-1974 versus 1955-1959, *J. Geophys. Res.*, **94**, 6091-6131, 1989.
- Lindzen, R.S., and B. Farrell, Some realistic modifications of simple climate models, *J. Atmos. Sci.*, **34**, 1487-1501, 1977.
- Lindzen, R.S., and B. Farrell, Reply (to Warren and Schneider), *J. Atmos. Sci.*, **37**, 900-902, 1980.
- Lorenz, E.N., Forced and free variations of weather and climate, *J. Atmos. Sci.*, **36**, 1367-1376, 1979.
- Manabe, S., and R.J. Stouffer, Two stable equilibria of a coupled ocean-atmosphere model, *J. Clim.*, **1**, 841-866, 1988.
- Marotzke, J., Instabilities and multiple steady states of the thermohaline circulation, in *Oceanic Circulation Models: Combining Data and Dynamics*, NATO ASI Ser., edited by D.L.T. Anderson and J. Willebrand, 501-511 pp., Kluwer Acad., 1989.
- McCartney, M.S., Recirculating components of the deep boundary current of the northern North Atlantic, *Prog. Oceanogr.*, **29**, 283-383, 1992.
- Mikolajewicz, U. and E. Maier-Reimer, Mixed boundary conditions in ocean general circulation models and their influence on the stability of the model's conveyor belt, *J. Geophys. Res.*, **99**, 22,633-22,644, 1994.
- North, G.R., Theory of energy balance climate models, *J. Atmos. Sci.*, **32**, 2033-2043, 1975a.
- North, G.R., Analytical solution to a simple climate model with diffusive heat transport, *J. Atmos. Sci.*, **32**, 1301-1307, 1975b.
- North, G.R., J.G. Mengel, and D.A. Short, Simple energy balance model resolving the seasons and the continents: Application to the Astronomical theory of the ice ages, *J. Geophys. Res.*, **88**, 6576-6586, 1983.
- Oberhuber, J.M., An atlas based on the "COADS" data set: The budgets of heat, buoyancy and turbulent kinetic energy at the surface of the global ocean, Max Planck Inst. for Meteorol., *Rep. 15*, Hamburg, Germany, 1988.
- Pacanowski, R., K. Dixon and A. Rosati, The G.F.D.L. modular ocean model users guide, *GFDL Ocean Group Tech. Rep. 2*, 46 pp., Geophys. Fluid Dyn., Princeton, N.J., 1993.
- Peixoto, J.P., and A. H. Oort, *Physics of Climate*, 520 pp. Am. Inst. of Phys., New York, 1992.
- Power, S.B., and R. Kleeman, Surface heat flux parameterization and the response of ocean general circulation models to high latitude freshening, *Tellus*, **46**, 86-95, 1994.
- Rahmstorf, S., and J. Willebrand, The role of temperature feedback is stabilizing the thermohaline circulation, *J. Phys. Oceanogr.*, **25**, 787-805, 1995.
- Ramanathan, V., The role of Earth radiation budget studies in climate and general circulation research, *J. Geophys. Res.*, **92**, 4075-4095, 1987.
- Sausen, R., K. Barthel, and K. Hasselmann, Coupled ocean-atmosphere models with flux corrections, *Clim. Dyn.*, **2**, 154-163, 1988.
- Schmitt, R.W., P.S. Bogden, and C.E. Dorman, Evaporation minus precipitation and density fluxes for the North Atlantic, *J. Phys. Oceanogr.*, **19**, 1208-1221, 1989.
- Schmitz, W.J., On the interbasin-scale thermohaline circulation, *Rev. Geophys.*, **33**, 151-173, 1995.
- Seager, M., A SLAP for the masses, *Tech. Rep. UCRL-100267*, Lawrence Livermore Natl. Lab., Livermore Calif., 1988.
- Sellers, W.D., *Physical Climatology*, 272 pp., Univ. of Chicago, Chicago, 1965.
- Sellers, W.D., A global climatic model based on the energy balance of the Earth-atmosphere system, *J. Appl. Meteorol.*, **8**, 392-400, 1969.
- Semtner, A.J., A model for the thermodynamic growth of sea ice in numerical investigations of climate, *J. Phys. Oceanogr.*, **6**, 379-389, 1976.

- Smith, S.D., Coefficients for sea surface wind stress, heat flux, and wind profiles as a function of wind speed and temperature, *J. Geophys. Res.*, **93**, 15,467-15,472, 1988.
- Stocker, T.F., D.G. Wright, and L.A. Mysak, A zonally averaged, coupled ocean-atmosphere model for paleoclimate studies, *J. Clim.*, **5**, 773-797, 1992.
- Thompson, S.J., and S.G. Warren, Parameterization of outgoing infrared radiation derived from detailed radiative calculations, *J. Atmos. Sci.*, **39**, 2667-2680, 1982.
- Trenberth, K.E., Recent observed interdecadal climate changes in the Northern Hemisphere, *Bull. Am. Meteorol. Soc.*, **71**, 988-993, 1990.
- Trenberth, K.E., and J.W. Hurrell, Decadal atmosphere-ocean variations in the Pacific, *Clim. Dyn.*, **9**, 303-319, 1994.
- Tziperman, E., J.R. Toggweiler, Y. Feliks, and K. Bryan, Instability of the thermohaline circulation with respect to mixed boundary conditions: Is it really a problem for realistic models?, *J. Phys. Oceanogr.*, **24**, 217-232, 1994.
- Weaver, A.J., and T.M.C. Hughes, On the incompatibility of ocean and atmosphere models and the need for flux adjustments, *Clim. Dyn.*, **12**, 141-170, 1996.
- Weaver, A.J., S.M. Aura, and P.G. Myers, Interdecadal variability in an idealized model of the North Atlantic, *J. Geophys. Res.*, **99**, 12,423-12,441, 1994.
- Weaver, A.J., and E.S. Sarachik, Evidence for decadal variability in an ocean general circulation model, *Atmos. Ocean*, **29**, 197-231, 1991.
- Weaver, A.J., E.S. Sarachik, and J. Marotzke, Freshwater flux forcing of decadal and interdecadal oceanic variability, *Nature*, **353**, 836-838, 1991.
- Weisse, R., U. Mikolajewicz, and E. Maier-Reimer, Decadal variability of the North Atlantic in an ocean general circulation model, *J. Geophys. Res.*, **99**, 12,411-12,421, 1994.
- Wigley, T.M.L., and T.P. Barnett, Detection of the greenhouse effect in the observations, in *Climate Change: The IPCC Scientific Assessment*, edited by J.T. Houghton, G.J. Jenkins, and J.J. Ephraums, pp. 239-255, Cambridge Univ. Press, New York, 1990.
- Zhang, S., R.J. Greatbatch, and C.A. Lin, A re-examination of the polar halocline catastrophe and implications for coupled ocean-atmosphere modeling, *J. Phys. Oceanogr.*, **23**, 287-299, 1993.

Augustus F. Fanning and Andrew J. Weaver, School of Earth and Ocean Sciences, University of Victoria, P.O. Box 1700, Victoria, B.C., V8W 2Y2 Canada.

(Received December 7, 1994; revised February 7, 1996; accepted March 20, 1996.)